

Numerical simulation of single- and multi-mode Rayleigh–Taylor instability with surface tension in two dimensions

Suyeon Shin^a, Sung-Ik Sohn^{b,*}, Woonjae Hwang^a

^a Division of Applied Mathematical Sciences, Korea University, Sejong 30019, Republic of Korea

^b Department of Mathematics, Gangneung-Wonju National University, Gangneung 25457, Republic of Korea

ARTICLE INFO

Article history:

Received 18 April 2021

Received in revised form 12 August 2021

Accepted 2 October 2021

Available online 21 October 2021

Keywords:

Rayleigh–Taylor instability

Surface tension

Mixing

Vortex sheet

ABSTRACT

In this paper, we study the long-time evolutions of the single- and multi-mode Rayleigh–Taylor instability with surface tension in two dimensions by using the vortex sheet model. Applying a spectrally accurate numerical method, we investigate the effects of surface tension and density jump on the instability in various regimes of parameters. Complex phenomena of pinching, capillary waves, elongation, and roll-up appear at the interfaces. For a single-mode interface, surface tension retards the growths of bubble and spike. The effect of surface tension on the bubble and spike velocity is generally small but is large for a spike of an infinite density ratio. For multi-mode interfaces, we focus on an infinite density ratio. We show that bubbles grow with the scaling law $h = \alpha g t^2$ even in the presence of surface tension, while spikes follow the scaling law weakly. It is found that both the growth rates of bubbles and spikes decrease with surface tension and the growth rate of spikes decreases larger than that of bubbles. The growth rate of the bubble front is in agreements with results of previous numerical simulations and experiments.

© 2021 The Author(s). Published by Elsevier Masson SAS. This is an open access article under the CC BY-NC-ND license (<http://creativecommons.org/licenses/by-nc-nd/4.0/>).

1. Introduction

Rayleigh–Taylor (RT) instability occurs when a heavy fluid is supported by a lighter fluid in a gravitational field [1,2]. A characteristic of RT instability is fingers, known as bubbles and spikes, of each phase extending into the region occupied by the opposite phase. The RT instability with initial random perturbations results in the bubble merger and turbulent mixing [3]. The RT instability plays an important role in a wide range of engineering, geophysical and astrophysical flows. To investigate the dynamics of this instability, extensive research effort has been expended over the last decades. A comprehensive review on the RT instability is provided in [3–5].

The RT instability arises commonly with surface tension. The evolution of RT instability with surface tension exhibits a variety of interesting behaviors such as pinching and break-up [6,7]. At the linear stage of the instability, it is well known that surface tension produces a cut-off wave number and stabilizes high modes [8]. Sohn [9] studied the effects of surface tension on the nonlinear evolution of RT instability from the potential-flow model and found that surface tension reduces the asymptotic velocity of a single-mode bubble. Although agreement of the asymptotic bubble velocity between the model and a numerical result was demonstrated in [9] for a single case of surface

tension with an infinite density ratio, further validation studies are required for a wide regime of parameters. In this paper, we perform numerical simulations for the single-mode RT instability to investigate the effects of surface tension and density jump in various parameters, particularly on the late-time velocity of bubble and spike.

The evolution of unstable interfaces with initial random perturbations are much more complicated than that of single mode. A central issue in the turbulent mixing by RT instability is the scaling law for the growth of the mixing zone. It has been found that the bubble front in the RT mixing grows self-similarly as

$$h_b = \alpha_b \frac{\rho_1 - \rho_2}{\rho_1 + \rho_2} g t^2. \quad (1)$$

The coefficient α_b is generally insensitive to the density ratio [5, 10–12], where ρ_1 and ρ_2 are the densities of heavy and light fluids, respectively, and g is the gravitation acceleration. The spike has a similar scaling law as the bubble, but weakly than bubble. The growth rate of spikes is larger than that of bubbles for moderate to large density ratios, i.e. $\alpha_s > \alpha_b$, and α_s increases with the density ratio. When surface tension is present at the interface, one may question several issues on the RT mixing that are not fully discovered yet: Do the bubble and spike growths of the RT mixing in the presence of surface tension follow the scaling law (1)? If they do, how much does the growth coefficient α_b and α_s increase or decrease?

* Corresponding author.

E-mail address: sohnsi@gwnu.ac.kr (S.-I. Sohn).

There have been only a few studies on the effect of surface tension on the multi-mode RT instability [10,13–17], although numerous researches have been carried out for RT mixing [5]. Moreover, some of these studies reported contrasting results on the growth rate of the mixing zone. From LEM (Linear Electric Motor) experiments, Dimonte and Schneider [10] found that the mixing rate of RT instability increases when surface tension is given, attributing the increase primarily to the enhanced meniscus at the wall. George et al. [15], and Young and Ham [16] conducted full numerical simulations for RT mixing with surface tension and showed that surface tension reduces the effective mixing rate. The main purpose of this paper is to investigate the abovementioned issues and clarify the contrasting results of previous studies.

A number of numerical simulations have been conducted for the RT mixing. Simulations using direct numerical simulation (DNS) and large eddy simulation (LES) for Navier–Stokes equations have been performed by Mueschke and Schilling [18], Youngs [19], Zhou and Cabot [20], and Yilmaz [21], listing only a few. For interface tracking, several different methods such as the front tracking method [15,22], levelset method [16], and phase-field model [23] were used. A direct numerical simulation of the three-dimensional RT mixing requires a huge number of grid points, to well resolve the small scale motions, and this is a daunting task; A numerical result of the RT mixing of high accuracy is still lacking. In these regards, it is desirable to study numerical simulations in two dimensions, while recognizing that the dynamics of the two-dimensional RT mixing is substantially different from that in three dimensions [24–27].

We conduct numerical computations of single- and multi-mode RT instability with surface tension, in two dimensions, from the vortex sheet model. For numerical computations, we employ a spectrally accurate numerical method for the vortex sheet model, which was previously developed for Kelvin–Helmholtz (KH) instability by the authors [28,29]. In this method, the interface is considered as a set of point vortices and these vortices are computed in Lagrangian manner by using a boundary integral, not solving differential equations in the whole domain. It should be emphasized that no regularization parameter is used in our computation, while the “ δ -parameter” is typically used for the computation of the vortex sheet when surface tension is absent [30,31]. Therefore, our spectral method provides a highly accurate solution for the nonlinear evolution of the interface. Note that the vortex sheet model has not been applied to simulate the multi-mode RT instability, except a result with only a few modes by Tryggvason [32].

Numerical computations for KH and RT instabilities with surface tension by using the vortex sheet model have been studied by several authors [6,7,33,34]. A key difficulty in the development of a numerical method for a vortex sheet with surface tension is to remove the aliasing instability in the highest wavenumbers. A major breakthrough in this regard was achieved by Hou, Lowen-grub and Shelley [33,34], who succeeded in the long-time computation of vortex sheets with surface tension. They presented a sophisticated implicit time-integration method, using small-scale decomposition, and employed a Fourier filter to remove the aliasing instability in the highest wavenumbers. The authors [28,29] adopted their numerical method and implemented it in a simple and explicit manner.

In Section 2, we describe the vortex sheet model with density jump and surface tension and present the numerical method for the vortex sheet motion briefly. Numerical results for the evolution of the single-mode RT instability for various density ratios and surface tensions are presented in Section 3, and results for the evolution of the multi-mode RT instability are presented in Section 4, focusing on the case of infinite density ratio. Section 5 gives conclusions.

2. Vortex sheet model

2.1. Model description

We consider the interface as a vortex sheet across which the tangential velocity is discontinuous. The fluids are assumed as inviscid, incompressible, and irrotational. The upper fluid is heavier than the lower fluid. The location of the vortex sheet is given by $\mathbf{X}(e, t) = (x(e, t), y(e, t))$ where e parametrizes the curve. The flow of each fluid is governed by the Euler equation:

$$\frac{\partial \mathbf{u}_i}{\partial t} + (\mathbf{u}_i \cdot \nabla) \mathbf{u}_i = -\frac{1}{\rho_i} \nabla p_i - g \mathbf{y}, \quad i = 1, 2, \quad (2)$$

where ρ_i is the density of the fluid and p_i is the pressure in the fluid. The upper fluid is denoted by 1 and the lower fluid is denoted by 2. We denote \mathbf{n} and \mathbf{s} by the unit normal and tangent vectors to the interface, respectively.

The evolution of the interface is given by

$$\frac{\partial \mathbf{X}}{\partial t} = U \mathbf{n} + T \mathbf{s}, \quad (3)$$

where U and T are the normal and tangential velocities of the interface, respectively. From the kinematic condition, the normal velocity is expressed as

$$U(e, t) = \mathbf{W}(e, t) \cdot \mathbf{n}, \quad (4)$$

where the average velocity on either side of the interface \mathbf{W} is given by the Birkhoff–Rott equation [35],

$$\mathbf{W}(e, t) = \frac{1}{2\pi} \text{P.V.} \int \frac{(\mathbf{X}(e, t) - \mathbf{X}(e', t))^\perp}{|\mathbf{X}(e, t) - \mathbf{X}(e', t)|^2} \gamma(e', t) de'. \quad (5)$$

Here, P.V. represents the principal value integral and $\mathbf{X}^\perp = (-y, x)$. The tangential velocity is decomposed into

$$T(e, t) = \mathbf{W}(e, t) \cdot \mathbf{s} + T^A(e, t), \quad (6)$$

where T^A is an arbitrary tangential velocity and its choice specifies the motion of the parametrization of the interface. Then, the evolution of the sheet is written as

$$\frac{\partial \mathbf{X}}{\partial t} = \mathbf{u} = \mathbf{W} + T^A \mathbf{s}. \quad (7)$$

The unnormalized vortex sheet strength is defined by

$$\gamma(e, t) = \frac{\partial \Gamma}{\partial e}(e, t), \quad (8)$$

where Γ is the circulation on the interface. It gives the tangential velocity difference across the interface by

$$\tilde{\gamma}(e, t) \equiv \frac{\gamma(e, t)}{s_e} = (\mathbf{u}_2 - \mathbf{u}_1) \cdot \mathbf{s}, \quad (9)$$

where $s_e = \sqrt{x_e^2 + y_e^2}$ is the arc-length metric, and \mathbf{u}_1 and \mathbf{u}_2 are the velocities on either side of the sheet. The velocity jump $\tilde{\gamma}$ is called the true vortex sheet strength. The velocities on either side of the interface are written as

$$\mathbf{u}_1 = \mathbf{W} - \frac{\gamma}{2s_e} \mathbf{s} = \mathbf{u} - \left(\frac{\gamma}{2s_e} + T^A \right) \mathbf{s}, \quad (10a)$$

$$\mathbf{u}_2 = \mathbf{W} + \frac{\gamma}{2s_e} \mathbf{s} = \mathbf{u} + \left(\frac{\gamma}{2s_e} - T^A \right) \mathbf{s}. \quad (10b)$$

The pressure difference on the interface is given by the Laplace law,

$$p_2 - p_1 = \sigma \kappa(e, t) = \sigma \frac{x_e y_{ee} - x_{ee} y_e}{(x_e^2 + y_e^2)^{3/2}}, \quad (11)$$

where σ and κ represent the surface tension and curvature of the interface, respectively. From the Euler equation on the interface

and the Laplace law, one can obtain the equation for the vortex sheet strength,

$$\frac{\partial \gamma}{\partial t}(e, t) = 2A \left(s_e \frac{\partial \mathbf{W}}{\partial t} \cdot \mathbf{s} + \frac{1}{8} \frac{\partial}{\partial e} \left(\frac{\gamma}{s_e} \right)^2 - T^A \mathbf{W}_e \cdot \mathbf{s} \right) + \frac{\sigma}{\rho_{av}} \kappa_e + \frac{\partial}{\partial e} \left(T^A \frac{\gamma}{s_e} \right) + 2A g y_e, \quad (12)$$

where $A = (\rho_1 - \rho_2)/(\rho_1 + \rho_2)$ is the Atwood number and $\rho_{av} = (\rho_1 + \rho_2)/2$. Eqs. (3) and (12) with (5) determine the evolution of the vortex sheet in the presence of surface tension, once T^A is specified. The Lagrangian frame corresponds to choosing the tangential velocity of the interface to be the average of the tangential fluid velocity on either side. In other words, the Lagrangian frame chooses $T = \mathbf{W} \cdot \mathbf{s}$, or $T^A = 0$. Instead of this frame, we take a special choice of the tangential velocity, which is explained shortly.

The role of surface tension is illustrated by considering first the linearized equations of motion to a flat interface. The flat interface $\mathbf{X}(e, t) = (e, 0)$ and $\gamma(e, t) = 0$ is an equilibrium solution of this problem. Let the interface be disturbed by $x(e, t) = e + \epsilon x^\epsilon(e, t)$, $y(e, t) = \epsilon y^\epsilon(e, t)$, and $\gamma(e, t) = \epsilon \gamma^\epsilon(e, t)$, with $\epsilon \ll 1$. Under the assumption that the perturbed solution is of the form $\exp(ik e + \lambda t)$, the linearized system of Eqs. (3), (5) and (12) gives the growth rate

$$\lambda(k) = \pm \sqrt{Agk - \frac{\sigma}{\rho_1 + \rho_2} k^3}. \quad (13)$$

Therefore, the interface is unstable for $k < k_c$ and is dispersive for $k \geq k_c$, where the critical wave number is

$$k_c = \sqrt{\frac{\rho_1(1-r)g}{\sigma}}, \quad (14)$$

and $r = \rho_2/\rho_1$ is the density ratio. The wavenumber of maximum growth is $k_{\max} = k_c/\sqrt{3}$. The growth rate (13) of our model recovers the result of the linear stability analysis in Chandrasekhar [8].

2.2. Numerical method

We use the numerical method for a vortex sheet with density jump and surface tension, which was previously developed by the authors [29]. Since the only difference of the physical setting from [29] is the inclusion of gravitational acceleration, the numerical method is explained briefly herein.

We assume a periodic vortex sheet of period D and express the equation in the complex form. The location of the interface is denoted as $z(e, t) = x(e, t) + iy(e, t)$, and the average velocity of the interface as $w = u + iv$. After scaling by the length scale D , time scale $\sqrt{D/Ag}$ and velocity scale \sqrt{AgD} , the Birkhoff–Rott equation and Eq. (12) are non-dimensionalized as

$$w^*(e, t) = \frac{1}{2i} \text{P.V.} \int_0^1 \gamma(e', t) \cot(\pi(z(e, t) - z(e', t))) de', \quad (15)$$

$$\frac{\partial \gamma}{\partial t}(e, t) = 2A \left[(u_t x_s + v_t y_s) s_e + \frac{1}{8} \frac{\partial}{\partial e} \left(\frac{\gamma}{s_e} \right)^2 - T^A (u_e x_s + v_e y_s) \right] + \frac{1}{Bo} \kappa_e + \frac{\partial}{\partial e} \left(T^A \frac{\gamma}{s_e} \right) + 2y_e, \quad (16)$$

where $*$ denotes the complex conjugate. Here, the Bond number is defined as

$$Bo = \frac{A \rho_{av} g D^2}{\sigma}. \quad (17)$$

The interface is discretized by $(x_j, y_j) = (x(e_j, t), y(e_j, t))$, $0 \leq e_j \leq 1$, where $e_j = jh$ and $h = 1/N$ is the uniform spacing.

We approximate integral (15) by applying the alternating point quadrature, which is of spectral accuracy [36],

$$w_j^* = \frac{2h}{2i} \sum_{\substack{m=0 \\ m+j=\text{odd}}}^{N-1} \gamma_m \cot(\pi(z_j - z_m)). \quad (18)$$

Eq. (16) is the Fredholm integral equation of second kind for γ_t , because $w_t = (u_t, v_t)$ is a function of γ_t . Here, it is solved by iteration until convergence within a tolerance level of 10^{-13} at each time step. We calculate the spacial derivatives in Eq. (16) using fast Fourier transformation (FFT), to maintain the spectral accuracy. For time-advancing, Eqs. (15) and (16) are integrated by using the classical fourth-order Runge–Kutta method.

The spectral method based on the alternating point quadrature is not free from the aliasing instability in the highest wavenumbers. The aliasing instability is removed by using a Fourier filter [34]. We also apply a different kind of filtering, called the Krasny filter, which sets the Fourier amplitudes under a given tolerance to zero [37]. The Krasny filter controls the spurious growth of round-off errors. These two filters are applied at each time step.

Next, we discuss the choice of the tangential velocity on the interface. The choice of the tangential velocity affects the distribution of vortex points on the interface. The Lagrangian frame, $T^A = 0$, is easy to implement but is not convenient to control the resolution of the interface. According to Hou et al. [33], $s_e(e, t)$ is a constant in e at time t when the tangential velocity T^A is selected as

$$T^A(e, t) = -\mathbf{W} \cdot \mathbf{s} + \int_0^e \theta'_e U de' - e \int_0^1 \theta'_e U de', \quad (19)$$

where θ is the tangent angle to the interface. This choice of the tangential velocity keeps the vortex points equally spaced in arc-length everywhere along the interface and is called as the uniform parametrization frame. Eq. (19) is rewritten in terms of the primitive variables x and y as

$$T^A(e, t) = -\mathbf{W} \cdot \mathbf{s} + \int_0^e \kappa s'_e U de' - e \int_0^1 \kappa s'_e U de', \quad (20)$$

from the relation $\theta_s = \theta_e/s_e = \kappa$. In summary, the evolution of the vortex sheet in the uniform parametrization frame is calculated by Eqs. (15) and (16) with (20).

3. Results for single-mode interfaces

We present the evolution of the single-mode RT instability by using the numerical method described in the previous section. The initial condition of the position and vortex sheet strength is given by

$$x(e, 0) = e, \quad y(e, 0) = a_0 \cos(2\pi e), \quad \gamma(e, 0) = 0, \quad (21)$$

for $0 \leq e \leq 1$. The initial amplitude is set to $a_0 = 0.08$. In all the computations in this section, the number of points is given by $N = 1024$ or 2048 , and the time step is set to $\Delta t = 10^{-4}$ for $N = 1024$ and $\Delta t = 5 \times 10^{-5}$ for $N = 2048$.

We first consider the parameters $A = 0.2$ and $Bo = 20$, which represent a small density jump and a large surface tension. The Atwood number $A = 0.2$ corresponds to a density ratio $1.5 : 1$. Fig. 1 shows the evolution of the interface for this case. In Fig. 1, roll-up does not appear on the interface, and the arms of the spike stretch outward, forming long fingers. Fig. 2 plots the (true) vortex sheet strength $\tilde{\gamma}$ and curvature κ . The sheet strength and curvature have two distinguished peaks, which correspond to the tips of the elongated fingers. The small peaks in the sheet strength and curvature correspond to the narrowed neck of the spike.

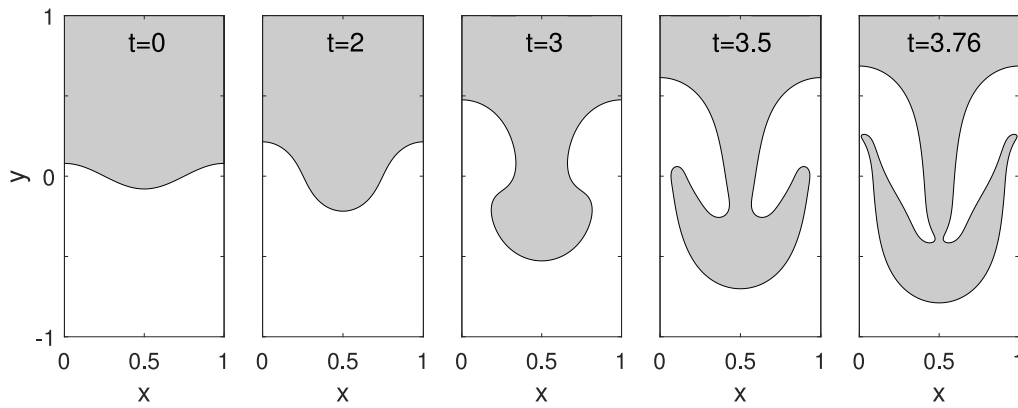


Fig. 1. Evolution of the interface for $A = 0.2$ and $Bo = 20$.

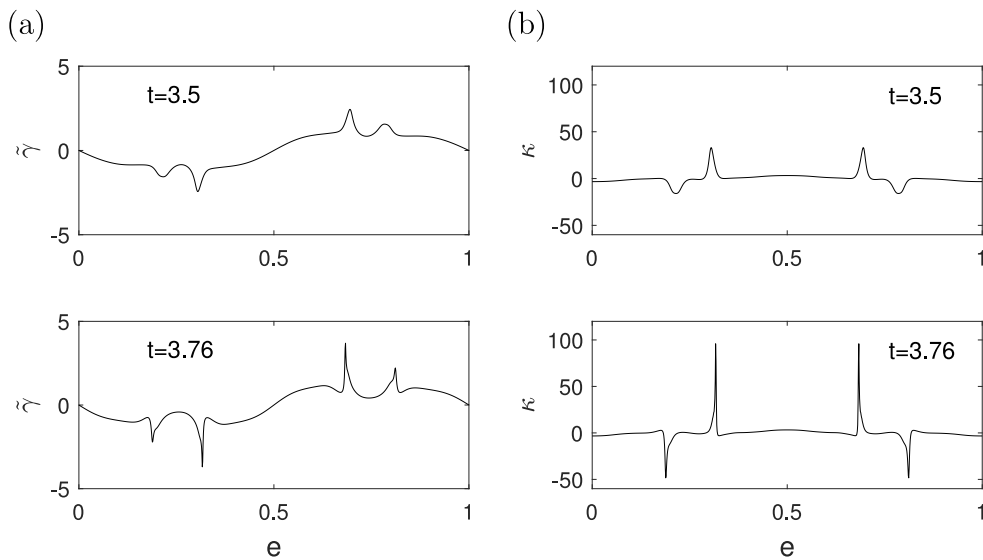


Fig. 2. (a) Vortex sheet strength and (b) curvature for $A = 0.2$ and $Bo = 20$.

We now consider various cases of Bond numbers and Atwood numbers. Fig. 3 shows a comparison of the interface for $Bo = 20, 50, 200$ with $A = 0.2$ at late times. For an intermediate Bond number $Bo = 50$, the outer boundary of the spike is rounded in shape and roll-up still does not appear on the interface; however, pinching is observed in the inner region of the spike, forming a jet. For a large Bond number $Bo = 200$, the spike has a roll-up and the interface collides with itself. The inner roll-up is pinched off and pinching occurs earlier than that of $Bo = 50$. We also find corrugations on the bottom of the outer boundary of the spike, which are “capillary waves” and are the dispersive effect of surface tension. Fig. 4 plots the vortex sheet strength at the interface. The sheet strength is strong when the interface is pinched and self-intersects, and also at the outer boundary of the spike. To examine the capillary waves, the curvature of the interface for $Bo = 200$ and $A = 0.2$ is plotted in Fig. 5. Only the left half of the interface is plotted, since the other half is symmetric. Fig. 5 shows that the peak of the curvature breaks into dispersive waves and the capillary waves are produced at about $t = 1.6$ and propagate outward from the center region.

Fig. 6 shows a comparison of the interface for varying Atwood numbers, $A = 0.2, 0.5, 0.8$ and 1 at late times. The Bond number is fixed to $Bo = 200$. As the Atwood number increases, the roll-up of the interface becomes weaker and the arm of the spike becomes shorter. The interface of $A = 1$ (infinite density ratio) has no roll-up.

Fig. 7 shows the evolution of the interface at late times for $Bo = 20, 50, 200$ with $A = 1$. For all cases, the interface stretches long and forms a pendant drop in the spike front. The neck of the spike is narrowed and eventually pinched off. For a smaller surface tension, the interface is more elongated and the drop is smaller.

We next compare the velocity of the bubble and spike for varying surface tensions. Fig. 8 plots the bubble velocity for $Bo = 20, 50$, and 200 . Fig. 8(a) is for $A = 0.2$ and Fig. 8(b) is for $A = 1$. In Fig. 8(b), the result for $Bo = 10^5$ is also shown as a limiting case of zero surface tension. The bubble velocity converges to a constant at late times in all the cases and decreases slightly for smaller Bond numbers. For $Bo = 20$, we observe oscillations at early times, which is due to the effect of strong surface tension. Note that for a very large surface tension, the interface is stable and behaves like a standing wave [6]. Fig. 9 plots the spike velocity for $Bo = 20, 50$, and 200 . Fig. 9(a) is for $A = 0.2$ and Fig. 9(b) is for $A = 1$. The sign of the spike velocity is reversed. In Fig. 9(b), the result for $Bo = 10^5$ is also shown. The spike attains a constant velocity for $A = 0.2$, but increases linearly for $A = 1$, indicating free falling. For both cases, the spike velocity decreases for smaller Bond numbers. Interestingly, the decrease of the spike velocity by surface tension is large for $A = 1$. We conclude that surface tension retards the growths of the bubble and spike of single-mode.

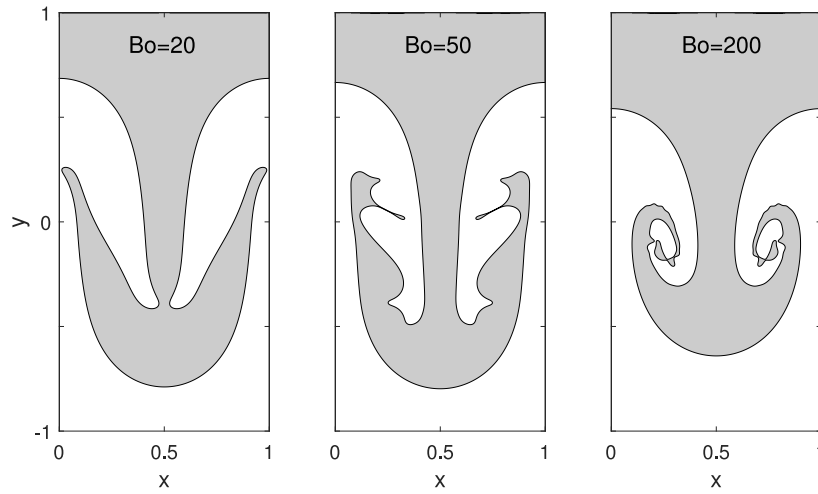


Fig. 3. Comparison of the interfaces for $Bo = 20, 50, 200$ with $A = 0.2$. The times are $t = 3.76$ for $Bo = 20$, $t = 2.48$ for $Bo = 50$, and $t = 1.90$ for $Bo = 200$.

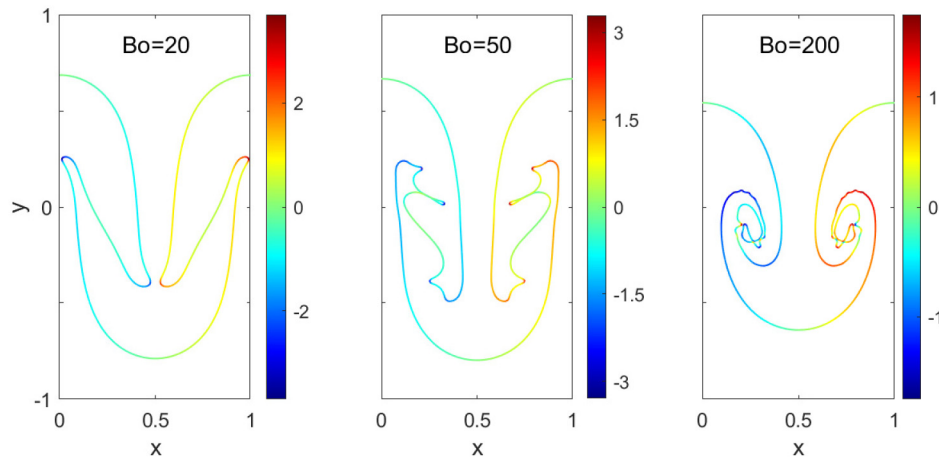


Fig. 4. Vortex sheet strength for $Bo = 20, 50, 200$ with $A = 0.2$.

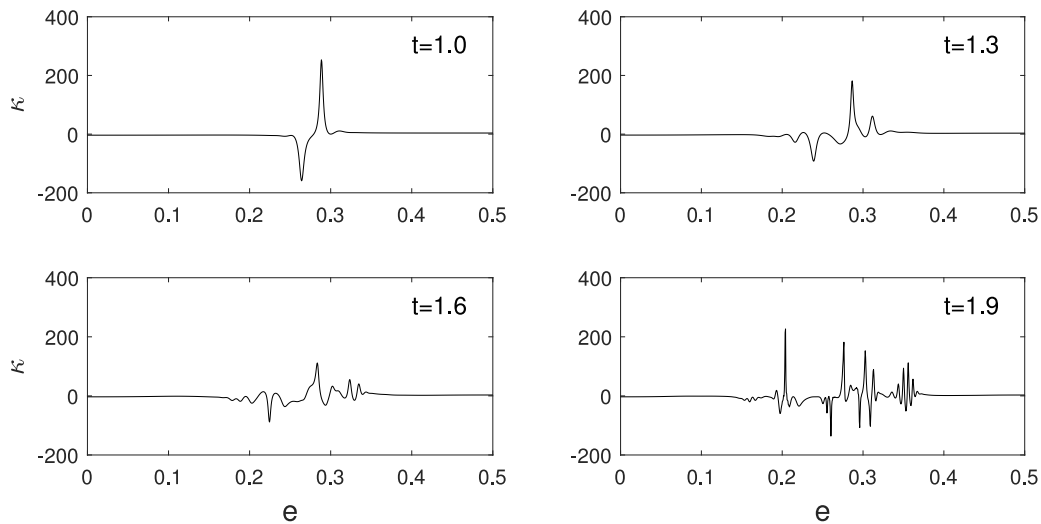


Fig. 5. Curvature of the interface for $Bo = 200$ and $A = 0.2$. Only the left half of the interface is shown by symmetry.

The asymptotic solution for the RT bubble velocity was obtained from a potential-flow model [9]:

$$U_{bb} \rightarrow \sqrt{\frac{2A}{3(1+A)} \frac{g}{k} - \frac{k}{9} \frac{\sigma}{\rho_1}} \quad (22)$$

The asymptotic bubble velocities of this solution and the numerical results are given in [Tables 1 and 2](#) for $A = 0.2$ and $A = 1$, respectively. The asymptotic bubble velocity of the numerical result is estimated from 0.5 before the final time. The model also

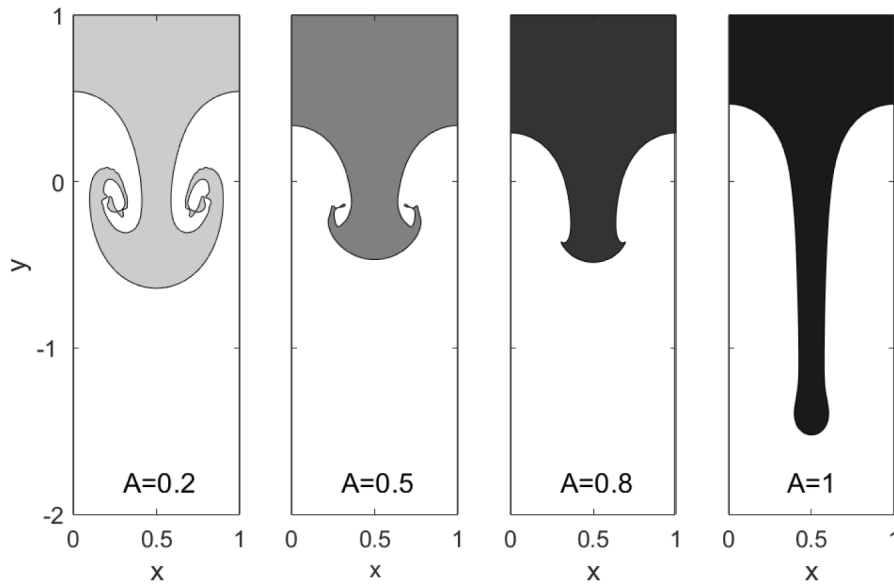


Fig. 6. Comparison of the interfaces for $A = 0.2, 0.5, 0.8$ and 1 at late times. The Bond number is fixed to $Bo = 200$. The times are $t = 1.92$ for $A = 0.2$, and $t = 1.3$ for $A = 0.5$, $t = 1.2$ for $A = 0.8$, and $t = 2$ for $A = 1$.

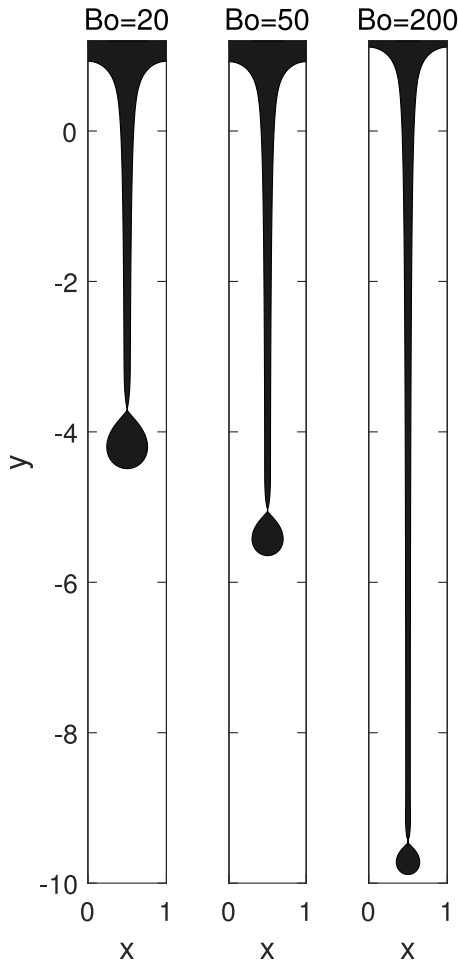


Fig. 7. Evolution of the interface for $Bo = 20, 50, 200$ and $A = 1$. The times are $t = 5.42$ for $Bo = 20$, $t = 4.21$ for $Bo = 50$ and $t = 4.89$ for $Bo = 200$.

predicts decrease of the bubble velocity as the Bond number is reduced, which is in reasonable agreements with the numerical

Table 1

Asymptotic bubble velocity for $Bo = 20, 50, 200$, and $A = 0.2$.

Bo	Model	Numer.
20	0.244	0.276 ± 0.002
50	0.277	0.293 ± 0.002
200	0.292	0.297 ± 0.004

Table 2

Asymptotic bubble velocity for $Bo = 20, 50, 200, 10^5$, and $A = 1$.

Bo	Model	Numer.
20	0.1887	0.2140
50	0.2146	0.2226
200	0.2265	0.2246
10^5	0.2303	0.2253

results. The difference between the model and the numerical result is however larger for smaller Bond number. For $Bo = 20$, the prediction of the model is 12% smaller than the numerical result for both cases of $A = 0.2$ and $A = 1$.

For $Bo = \infty$ (zero surface tension), the potential-flow model predicts the asymptotic bubble velocity: 0.297 for $A = 0.2$, and 0.230 for $A = 1$. The numerical result for $A = 1$ in Fig. 8(b) shows convergence in the limit of vanishing surface tension and is in good agreement with the asymptotic bubble velocity of the potential-flow model with $Bo = \infty$; The numerical result for $A = 0.2$ also shows the trend of convergence in reducing surface tension. Note that the numerical computation for $A < 1$ in the limit of zero surface tension suffers from appearance of a singularity at finite-time from Kelvin–Helmholtz instability [36,37] and thus a regularization method [30,31] should be applied to the model for the longtime computation. The result for the RT instability of $A = 0.2$ with zero surface tension by using a blob-regularization method can be found in [38]. On the other hand, there are several theoretical works on the asymptotic growth rate of RT bubble and spike in the absence of surface tension [4]. The multi-harmonic model [39] predicts the asymptotic bubble velocity: 0.332 for $A = 0.2$, and 0.230 for $A = 1$.

4. Results for multi-mode interfaces

We conduct simulations for the interface of initial multi-mode perturbations. For $A < 1$, the self-intersection and break-up

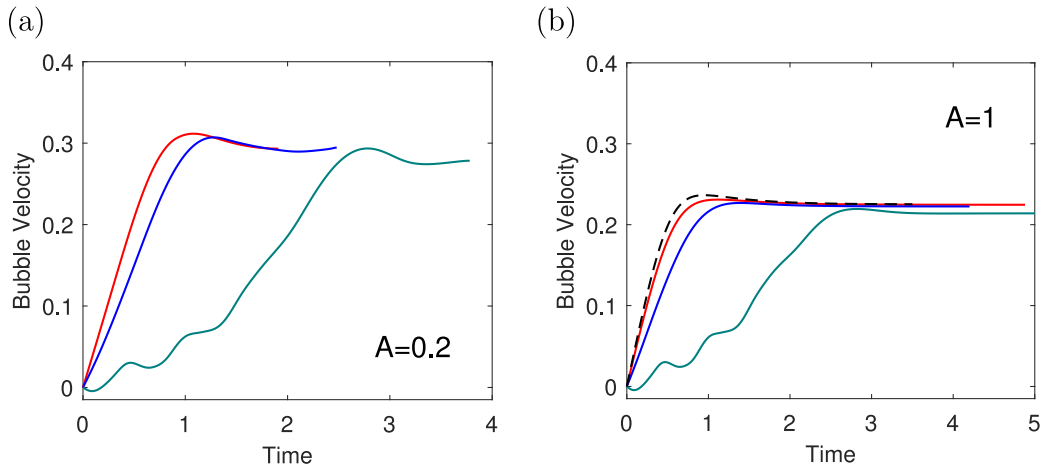


Fig. 8. Bubble velocity for $Bo = 20$ (green), $Bo = 50$ (blue), $Bo = 200$ (red). (a) $A = 0.2$ and (b) $A = 1$. In (b), the result for $Bo = 10^5$ (dashed black) is also shown as a limiting case of zero surface tension. (For interpretation of the references to color in this figure legend, the reader is referred to the web version of this article.)

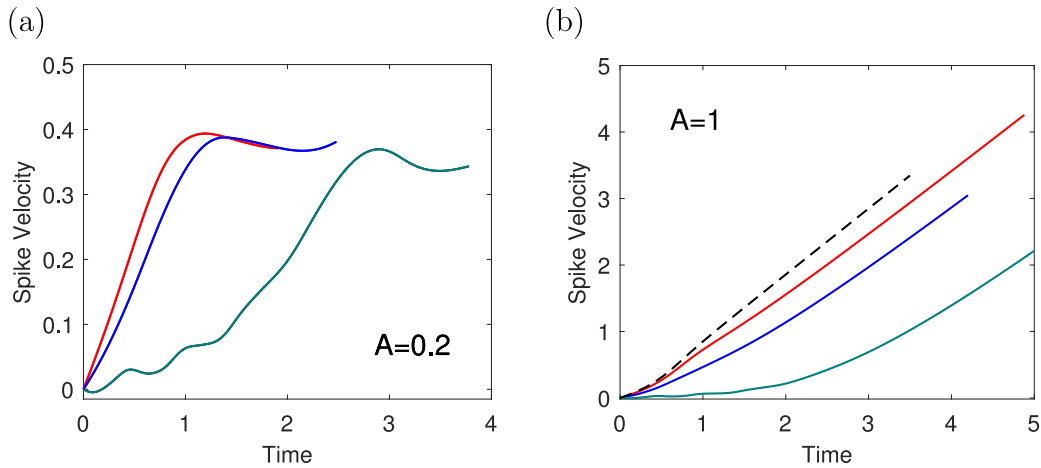


Fig. 9. Spike velocity for $Bo = 20$ (green), $Bo = 50$ (blue), $Bo = 200$ (red). (a) $A = 0.2$ and (b) $A = 1$. In (b), the result for $Bo = 10^5$ (dashed black) is also shown as a limiting case of zero surface tension. (For interpretation of the references to color in this figure legend, the reader is referred to the web version of this article.)

of the interface are common in the multi-mode RT instability, particularly for low and moderate Atwood numbers; however, the numerical method of the vortex sheet model has not been developed to handle these problems. We thus focus on the case of a large Atwood number, $A = 1$. The mode numbers are selected in the range from 5 to 20 for the simulation. The initial condition is given by

$$\begin{aligned} x(e, 0) &= e, \\ y(e, 0) &= \sum_{k=5}^{20} [a_k \cos(2\pi ke) + b_k \sin(2\pi ke)], \\ \gamma(e, 0) &= 0, \end{aligned} \quad (23)$$

for $0 \leq e \leq 1$, where a_k and b_k are chosen as Gaussian random variables, with a mean 0 and standard deviation 0.0001. This initial condition generates approximately 13–15 bubbles at the interface. In the multi-modes, considering the average length scale $\bar{D} = D/N_b$ where N_b is the average number of initial bubbles, we introduce a rescaled Bond number,

$$\bar{Bo} = \frac{1}{N_b^2} Bo. \quad (24)$$

For the simulations, we take Bond numbers, $\bar{Bo} = 1000$ and $\bar{Bo} = 50$, as two representative cases for small and large surface

tensions. The evolution of the interface with random perturbations for these two cases is shown in Fig. 10. The number of points and time step are given by $N = 2048$ and $\Delta t = 5 \times 10^{-5}$. As time progresses, the smaller bubbles shrink, retreat and merge into larger bubbles. The number of bubbles are thus reduced at late times. We observe 12 bubbles in the front of the interface for $\bar{Bo} = 1000$ and 10 bubbles for $\bar{Bo} = 50$ finally. The spikes for $\bar{Bo} = 1000$ fall further, forming long fingers, compared with those for $\bar{Bo} = 50$.

Fig. 11 plots the mixing front growth of bubbles and spikes vs. $Ag t^2$ for $\bar{Bo} = 1000, 83.3$, and 50. Fig. 11(a) shows that the bubble height decreases slightly for the larger surface tension. In Fig. 11(b), the sign of the spike height is reversed. The spike height also decreases for the larger surface tension, and the effect of surface tension is much larger than the bubbles. In Fig. 11, the linear fittings of the curves are also shown by dashed lines and agree well with the curves. This indicates that RT mixing in the presence of surface tension grows with scaling law (1).

We run more simulations for Bond numbers, $\bar{Bo} = 1000, 166.7, 83.3, 62.5$, and 50, with three different random perturbations. (Or, $\bar{Bo}^{-1} = 0.001, 0.006, 0.012, 0.016$, and 0.02.) The growth coefficients of the bubbles and spikes in these runs are shown in Fig. 12. To compare with other results, the growth coefficients are plotted with respect to the inverse Bond number. In Fig. 12(a), the growth rate of the bubbles is in the range of

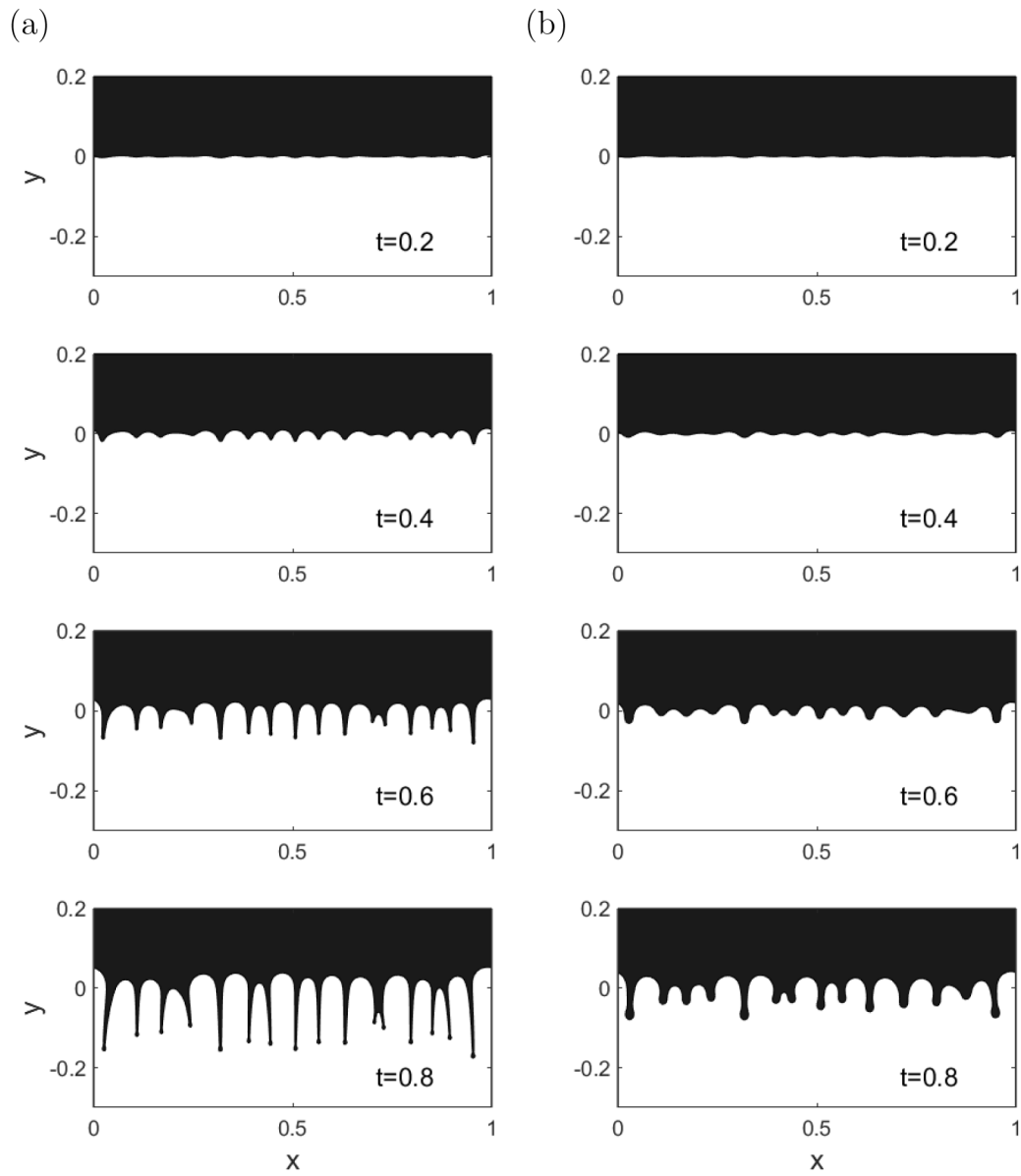


Fig. 10. Evolution of the interface with random perturbations for (a) $\overline{Bo} = 1000$ and (b) $\overline{Bo} = 50$.

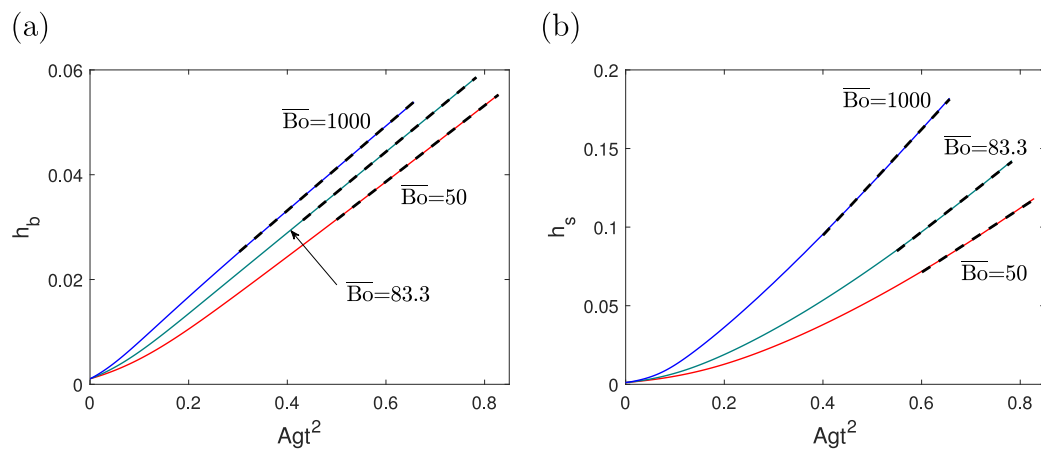


Fig. 11. Growth of the mixing front vs. Agt^2 for $\overline{Bo} = 1000, 83.3$ and 50 . (a) bubble height h_b , and (b) spike height h_s . The linear fitting of the curves are also shown by dashed lines.

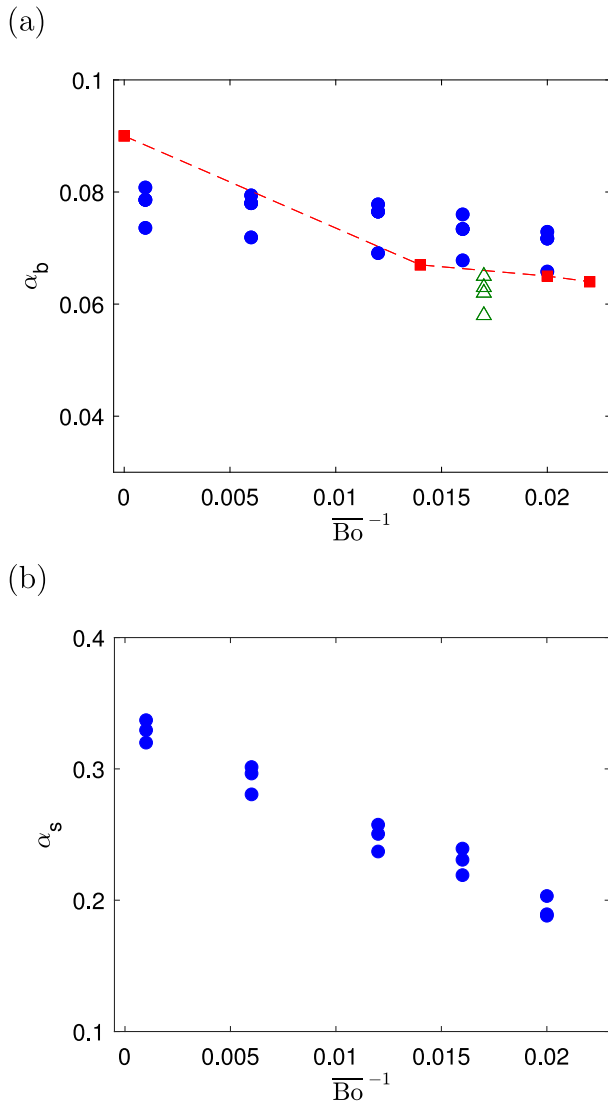


Fig. 12. Growth coefficients of (a) bubbles and (b) spikes vs. the inverse Bond number. The square represents the result of the front-tracking simulation [15], and the triangle represents the experimental data in Read [40].

0.065 – 0.081 and decreases slightly with the inverse Bond number. The growth rate of the bubbles is in good agreement with the result of the three-dimensional front tracking simulation by Glimm's group [15], which is denoted by the square in Fig. 12(a). We also compare with the result of a two-dimensional experiment by Read [40], shown by the triangle. The experimental values are slightly lower than our result, but indicates reasonable agreement. In Fig. 12(b), the growth rate of the spikes ranges from 0.18 to 0.34, which is much larger than that of the bubbles, and decreases significantly with surface tension. The growth rate ratios of the bubbles and spikes with the inverse Bond number is plotted in Fig. 13. It shows that the ratio of the growth coefficient is larger for a smaller surface tension.

Let us examine the growth rate of the mixing front more precisely. We define the effective growth rate as $\alpha_{\text{eff}} = h/Ag\tau^2$. Fig. 14 plots the effective growth rate of the bubble front for $\overline{Bo} = 1000$ and 50 for the three simulations. Fig. 14(a) shows that the growth rate of the bubbles indeed becomes constant when surface tension is very small. In Fig. 14(b), when surface tension increases, the growth rate of the bubbles decreases overall and slightly increases at late times. This indicates that even for a large

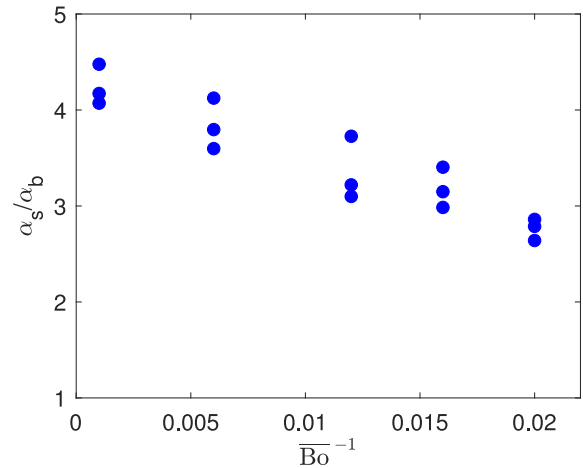


Fig. 13. Ratio of growth rates of bubbles and spikes.

surface tension, the bubble front still grows with the scaling law. Fig. 15 plots the effective growth rate of the spike front for the two Bond numbers. In Fig. 15(a), when surface tension is very small, the growth rate of the spikes increases, which means a weak adherence to the scaling law. In Fig. 15(b), for a large surface tension, the growth rate of the spikes reduces significantly overall and increases less compared with the case of a small surface tension in Fig. 15(a).

5. Conclusions

We have presented the evolution of the RT instability from the vortex sheet model and have investigated the dynamics of the single- and multi-mode interfaces for various regimes of surface tension. Highly accurate solutions for the interface evolution are obtained by applying a spectral method. Most previous studies of the vortex sheet model on the RT instability were limited to the single-mode interface. The main contribution of our study is the long-time computation of the multi-mode RT instability using the vortex sheet model for the first time.

Complex phenomena of pinching, capillary waves, elongation, and roll-up appear at the interfaces. For a single-mode interface, surface tension decelerates both the bubble and spike growth. The effect of surface tension on the bubble and spike velocity is small in general, but is large for the spike in the flow of an infinite density ratio.

The results for the interface of multi-mode perturbations, for $A = 1$, show the competition and merging of fingers, as well as pinching and elongation. We find that the bubble front grows with the scaling law even in the presence of surface tension, while the spike front follows the scaling law weakly. Both growth rates of bubbles and spikes decrease with surface tension. Nevertheless, the decrease of the growth rate of spikes is much larger than that of bubbles.

Our result for the multi-mode RT instability is consistent with the previous numerical simulations [15,16]. The different trend of the growth rate of the scaling law on surface tension between the numerical simulations and the LEM experiment [10] would be due to the effect of the solid wall. The numerical simulations usually use a periodic boundary condition, i.e. no solid wall, whereas the experiment is conducted on a solid container. The meniscus on the wall by the capillary effect elevates the fluid interface and may increase the mixing rate [41]. The influence of wall effects on the RT mixing is also illustrated in the tilted-rig experiment [42]. Besides, there might be more sources to

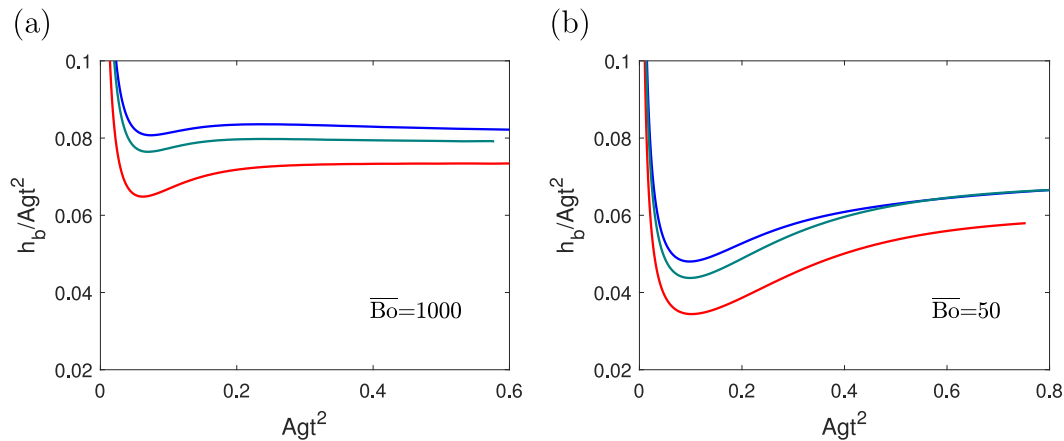


Fig. 14. Effective growth rate of bubbles for (a) $\overline{Bo} = 1000$, and (b) $\overline{Bo} = 50$.

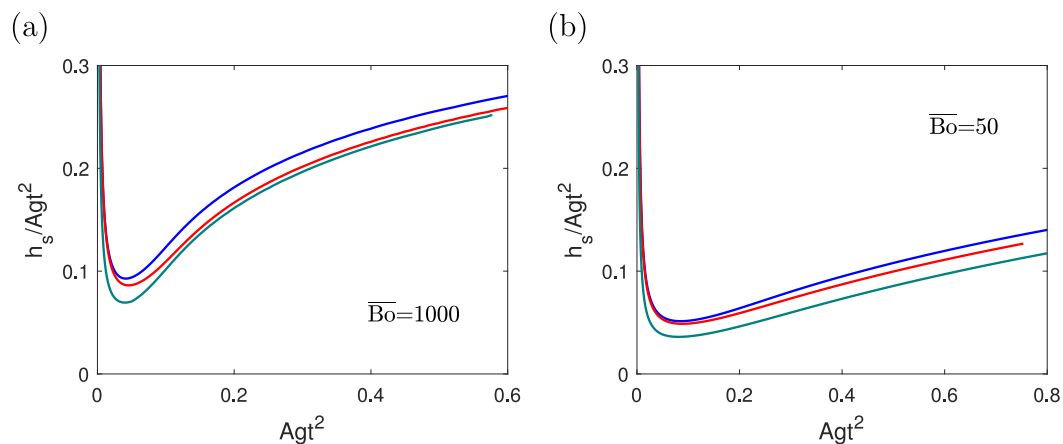


Fig. 15. Effective growth rate of spikes for (a) $\overline{Bo} = 1000$, and (b) $\overline{Bo} = 50$.

affect the growth rate in the experiment, e.g. compressibility and isothermality of fluids.

Several improvements of our numerical method remain for future works, including the implementation of the solid wall. To investigate the effect of surface tension on the RT mixing on a finite density ratio, the numerical method of the vortex sheet model should be extended to handle the self-collision and topological change of the interface. The vortex sheet model in this work concerns the RT instability in two dimensions and excludes the three dimensional effects such as vortex stretching. In fact, there have been only a few works on the vortex sheet model in three dimensions [43,44]. The numerical simulation of three-dimensional RT instability by using the vortex sheet model is an interesting and challenging subject.

Declaration of competing interest

The authors declare that they have no known competing financial interests or personal relationships that could have appeared to influence the work reported in this paper.

Acknowledgments

The authors thank the anonymous referees for their valuable comments. This research was supported by the National Research Foundation of Korea (NRF), South Korea grant funded by the Korea government (MSIT) under Grant Nos. NRF-2020R1I1A1A01056687 (S.S.), NRF-2018R1A2B6002164 (S.-I.S.), and NRF-2018R1D1A1B070481 (W. H.).

References

- [1] Lord Rayleigh, Investigation of the character of the equilibrium of an incompressible heavy fluid of variable density, *Proc. Lond. Math. Soc.* 14 (1883) 170–177.
- [2] G.I. Taylor, The instability of liquid surfaces when accelerated in a direction perpendicular to their planes I, *Proc. R. Soc. Lond. Ser. A Math. Phys. Eng. Sci.* 201 (1950) 192–196.
- [3] D. Sharp, An overview of Rayleigh–Taylor instability, *Physica D* 12 (1984) 3–10.
- [4] S.I. Abarzhi, Review of theoretical modelling approaches of Rayleigh–Taylor instabilities and turbulent mixing, *Phil. Trans. R. Soc. A* 368 (2010) 1809–1828.
- [5] Y. Zhou, Rayleigh–Taylor and Richtmyer–Meshkov instability induced flow, turbulence, and mixing. I, *Phys. Rep.* 720 (2017) 1–136.
- [6] H.D. Cenicerros, T.Y. Hou, Convergence of a non-stiff boundary integral method for interfacial flows with surface tension, *Math. Comp.* 67 (1998) 137–182.
- [7] C. Matsuoka, Vortex sheet motion in incompressible Richtmyer–Meshkov and Rayleigh–Taylor instabilities with surface tension, *Phys. Fluids* 21 (2009) 092107.
- [8] S. Chandrasekhar, *Hydrodynamic and Hydromagnetic Stability*, Oxford University Press, Oxford, 1961.
- [9] S.-I. Sohn, Effects of surface tension and viscosity on the growth rates of Rayleigh–Taylor and Richtmyer–Meshkov instabilities, *Phys. Rev. E* 80 (2009) 055302.
- [10] G. Dimonte, M. Schneider, Density ratio dependence of Rayleigh–Taylor mixing for sustained and impulsive acceleration histories, *Phys. Fluids* 12 (2000) 304–321.
- [11] G. Dimonte, et al., A comparative study of the turbulent Rayleigh–Taylor instability using high-resolution three-dimensional numerical simulations: The Alpha-Group collaboration, *Phys. Fluids* 16 (2004) 1668–1693.
- [12] A. Banerjee, W.N. Kraft, M.J. Andrews, Detailed measurements of a statistically steady Rayleigh–Taylor mixing layer from small to high Atwood numbers, *J. Fluid Mech.* 659 (2010) 127–190.

- [13] C. Cherfil, K.O. Mikaelian, Simple model for the turbulent mixing width at an ablating surface, *Phys. Fluids* 8 (1996) 522–535.
- [14] M. Chertkov, I. Kolokolov, V. Lebedev, Effects of surface tension on immiscible Rayleigh–Taylor turbulence, *Phys. Rev. E* 71 (2005) 055301.
- [15] E. George, J. Glimm, X.-L. Li, Y.-H. Li, X.-F. Liu, Influence of scale-breaking phenomena on turbulent mixing rates, *Phys. Rev. E* 73 (2006) 016304.
- [16] Y.N. Young, F.E. Ham, Surface tension in incompressible Rayleigh–Taylor mixing flow, *J. Turbul.* 7 (2006) 1–23.
- [17] S.-I. Sohn, S. Baek, Bubble merger and scaling law of the Rayleigh–Taylor instability with surface tension, *Phys. Lett. A* 381 (2017) 3812–3817.
- [18] J. Mueschke, O. Schilling, Investigation of Rayleigh–Taylor turbulence and mixing using direct numerical simulation with experimentally measured initial conditions. II. Dynamics of transitional flow and mixing statistics, *Phys. Fluids* 21 (2009) 014107.
- [19] D.L. Youngs, Rayleigh–Taylor mixing: Direct numerical simulation and implicit large eddy simulation, *Phys. Scr.* 92 (2017) 074006.
- [20] Y. Zhou, W.H. Cabot, Time-dependent study of anisotropy in Rayleigh–Taylor instability induced turbulent flows with a variety of density ratios, *Phys. Fluids* 31 (2019) 084106.
- [21] I. Yilmaz, Analysis of Rayleigh–Taylor instability at high atwood numbers using fully implicit, non-dissipative, energy-conserving large eddy simulation algorithm, *Phys. Fluids* 32 (2020) 054101.
- [22] J. Glimm, D.H. Sharp, T. Kaman, H. Lim, New directions for Rayleigh–Taylor mixing, *Philos. Trans. R. Soc. A* 371 (2013) 20120183.
- [23] J. Yang, H.G. Lee, J. Kim, Side wall boundary effect on the Rayleigh–Taylor instability, *Eur. J. Mech. B Fluids* 85 (2021) 361–374.
- [24] M. Chertkov, Phenomenology of Rayleigh–Taylor turbulence, *Phys. Rev. Lett.* 11 (2003) 115001.
- [25] A. Celani, A. Mazzino, L. Vozella, Rayleigh–Taylor turbulence in two dimensions, *Phys. Rev. Lett.* 96 (2006) 134504.
- [26] W. Cabot, Comparison of two- and three-dimensional simulations of miscible Rayleigh–Taylor instability, *Phys. Fluids* 18 (2006) 045101.
- [27] Q. Zhou, Temporal evolution and scaling of mixing in two-dimensional Rayleigh–Taylor turbulence, *Phys. Fluids* 25 (2013) 085107.
- [28] S. Shin, S.-I. Sohn, W. Hwang, Simple and efficient numerical methods for vortex sheet motion with surface tension, *Internat. J. Numer. Methods Fluids* 74 (2014) 422–438.
- [29] S. Shin, S.-I. Sohn, W. Hwang, Vortex simulations of the Kelvin–Helmholtz instability with surface tension in density-stratified flows, *Eur. J. Mech. B Fluids* 67 (2018) 168–177.
- [30] R. Krasny, Desingularization of periodic vortex sheet roll-up, *J. Comput. Phys.* 65 (1986) 292–313.
- [31] S.-I. Sohn, Two vortex-blob regularization models for vortex sheet motion, *Phys. Fluids* 26 (2014) 044105.
- [32] G. Tryggvason, Numerical simulations of Rayleigh–Taylor instability, *J. Comput. Phys.* 75 (1988) 253–282.
- [33] T.Y. Hou, J.S. Lowengrub, M.J. Shelley, Removing the stiffness from interfacial flows with surface tension, *J. Comput. Phys.* 114 (1994) 312–338.
- [34] T.Y. Hou, J.S. Lowengrub, M.J. Shelley, The long-time motion of vortex sheets with surface tension, *Phys. Fluids* 9 (1997) 1933–1954.
- [35] G. Birkhoff, Helmholtz and Taylor instability, in: *Proc. Symposia in Applied Mathematics*, Vol. XIII, American Mathematical Society, Providence, Rhode Island, 1962, pp. 55–76.
- [36] M.J. Shelley, A study of singularity formation in vortex-sheet motion by a spectrally accurate vortex method, *J. Fluid Mech.* 244 (1992) 493–526.
- [37] R. Krasny, A study of singularity formation in a vortex sheet by the point-vortex approximation, *J. Fluid Mech.* 167 (1986) 65–93.
- [38] S.-I. Sohn, Late-time vortex dynamics of Rayleigh–Taylor instability, *J. Phys. Soc. Japan* 80 (2011) 084401.
- [39] S.I. Abarzhi, J. Glimm, A.-D. Lin, Dynamics of two-dimensional Rayleigh–Taylor bubbles for fluids with a finite density contrast, *Phys. Fluids* 15 (2003) 2190–2197.
- [40] K.I. Read, Experimental investigation of turbulent mixing by Rayleigh–Taylor instability, *Physica D* 12 (1984) 45–58.
- [41] P.-G. de Gennes, F. Brochard-Wyart, D. Quere, *Capillarity and Wetting Phenomena*, Springer-Verlag, New York, 2004.
- [42] M.J. Andrews, D.L. Youngs, D. Livescu, T. Wei, Computational studies of two-dimensional Rayleigh–Taylor driven mixing for a tilted-rig, *ASME J. Fluids Eng.* 136 (2014) 091212.
- [43] K. Lindsay, R. Krasny, A particle method and adaptive treecode for vortex sheet motion in three-dimensional flow, *J. Comput. Phys.* 172 (2001) 879–907.
- [44] M.J. Stock, W.J.A. Dahm, G. Tryggvason, Impact of a vortex ring on a density interface using a regularized inviscid vortex sheet method, *J. Comput. Phys.* 227 (2009) 9021–9043.